electronics

MDPI

Article

Modeling and Accuracy Assessment of Determining the Coastline Course Using Geodetic, Photogrammetric and Satellite Measurement Methods: Case Study in Gdynia Beach in Poland

Francesco Giuseppe Figliomeni [1], Mariusz Specht [2,*], Claudio Parente [3], Cezary Specht [4] and Andrzej Stateczny [5]

[1] International PhD Programme "Environment, Resources and Sustainable Development", Department of Science and Technology, Parthenope University of Naples, 80143 Naples, Italy; francescogiuseppe.figliomeni001@studenti.uniparthenope.it
[2] Department of Transport and Logistics, Gdynia Maritime University, Morska 81-87, 81-225 Gdynia, Poland
[3] DIST—Department of Science and Technology, Parthenope University of Naples, 80143 Naples, Italy; claudio.parente@uniparthenope.it
[4] Department of Geodesy and Oceanography, Gdynia Maritime University, Morska 81-87, 81-225 Gdynia, Poland; c.specht@wn.umg.edu.pl
[5] Department of Geodesy, Gdańsk University of Technology, Gabriela Narutowicza 11-12, 80-233 Gdańsk, Poland; andrzej.stateczny@pg.edu.pl
* Correspondence: m.specht@wn.umg.edu.pl

Abstract: The coastal environment represents a resource from both a natural and economic point of view, but it is subject to continuous transformations due to climate change, human activities, and natural risks. Remote sensing techniques have enormous potential in monitoring coastal areas. However, one of the main tasks is accurately identifying the boundary between waterbodies such as oceans, seas, lakes or rivers, and the land surface. The aim of this research is to evaluate the accuracy of coastline extraction using different datasets. The images used come from UAV-RGB and the Landsat-9 and Sentinel-2 satellites. The method applied for extracting the coast feature involves a first phase of application of the Normalized Difference Water Index (NDWI), only for satellite data, and consequent application of the maximum likelihood classification, with automatic vectorization. To carry out a direct comparison with the extracted data, a coastline obtained through a field survey using a Global Navigation Satellite System (GNSS) device was used. The results are very satisfactory as they meet the minimum requirements specified by the International Hydrographic Organization (IHO) S-44. Both the UAV and the Sentinel-2 reach the maximum order, called the Exclusive order (Total Horizontal Uncertainty (THU) of 5 m with a confidence level of 95%), while the Landsat-9 falls into the Special order (THU of 10 m with a confidence level of 95%).

Keywords: coastline extraction; UAV; Landsat-9; Sentinel-2; GNSS

Citation: Figliomeni, F.G.; Specht, M.; Parente, C.; Specht, C.; Stateczny, A. Modeling and Accuracy Assessment of Determining the Coastline Course Using Geodetic, Photogrammetric and Satellite Measurement Methods: Case Study in Gdynia Beach in Poland. *Electronics* **2024**, *13*, 412. https://doi.org/10.3390/electronics13020412

Academic Editors: Yunda Yan, Dewei Yi, Hao Lu and Lan Gao

Received: 30 November 2023
Revised: 8 January 2024
Accepted: 15 January 2024
Published: 19 January 2024

1. Introduction

It is estimated that the total extension of the world coastline is approximately 504,000 km [1] and its malleability affects a large part of the human population and also the marine and terrestrial flora and fauna. Therefore, the detection and monitoring of this important resource has both an economic and social impact, also due to the effects of ongoing climate change.

The coastline is often defined as the physical transition between land and water [2,3]. Due to its very dynamic nature, it can be defined in several ways. The choice of the position of the coastline must be given on adequate spatial and temporal scales.

The most used definitions of coastline based on the time scale are instantaneous coastline, short-term coastline, and long-term coastline [4]. The instantaneous coastline is defined as the position of the land/sea separation line in an instant of time [5]. The

short-term coastline requires multiple locations of the line under consideration at the rate of several samples at a time, for a limited period [6]. Finally, the long-term coastline may require averaging the position of the line over a 10/20-year period of time [7]. Another possible approach would be to take the instantaneous coastline and correct it for tidal effects and seawater conditions [8]. However, most coastline survey methods focus on instantaneous coastline detection, which forms the basis for all coastlines analyses.

In recent years, several approaches were used to monitor coastline change due to uncontrolled erosion or accretion [9–11]. The methods to determine the position of the coastline can be divided into field survey methods or remote sensing data [12].

Field survey approaches are among the most widespread and involve the use of traditional topographic surveys, such as the acquisition of points with the Global Navigation Satellite System (GNSS) [13]. It allows us to acquire high-precision measurements of points along the line of interest. It is a low-cost approach, thanks also to modern technologies, and is independent of cloud cover and weather conditions, with rapid data processing methods. In addition, the accuracy of this survey also depends on the type of method used. Various GNSS methods applicable to coastline extraction exist and the most commonly used are relative kinematic (RK), real-time kinematic (RTK), and precise point positioning (PPP) methods [14]. However, when the area to be investigated is large, it requires a very long acquisition time so that there are an adequate number of points that allow the coastline to be generated. In any case, topographic surveys from the point of view of positional accuracy are currently the best; an example is the study conducted for coastal monitoring by Goncalves and Awange [14]. Using GNSS receivers applying different methods, they compared the three most commonly used approaches for GNSS-based shoreline monitoring (RK, RTK and PPP). The area investigated was the integrated coastal zone management of the state of Pernambuco in Brazil, and the findings highlight the issues and considerations in choosing a cost-effective GNSS method for mapping coastal changes. The results achieve a high accuracy for the best of the three (RTK) with a planimetric accuracy of approximately 0.01 m, while for the worst (PPP), it is 0.22 m.

As for remote sensing data for coastline extraction, it includes a large portion of methods that can be further divided into aerophotogrammetric/UAV surveys, radar or optical satellite imagery, and airborne Lidar. However, these approaches are increasingly widespread as they allow the coastline of a very large area to be determined in a short time. While on the one hand, methods that use remote sensing data allow the limitations of the classic topographic approach to be overcome, on the other hand, some of them may be expensive or may not achieve the precision of the previous ones.

In the literature we have several cases that analyze the results of methods with remote sensing data, and the accuracies are different. In the work conducted by Zanutta et al. [15], UAV photogrammetric techniques and GNSS techniques to obtain coastal changes due to natural and anthropogenic influences are compared. Multitemporal UAV surveys, of the coastal area of the Upper Adriatic, in Ravenna (Italy), were performed using UAVs supported by Ground Control Points (GCP) and Post Processed Kinematic (PPK). The results produced by the difference between the coordinates of the GCPs and those measured on the digital photogrammetric terrain models (DTMs) produced an *RMSE* of 0.10 m at worst and 0.02 m at best. These values are comparable with the accuracies of data acquired with topographic surveys.

By changing the acquisition tool, i.e., SAR (Synthetic Aperture Radar) rather than UAV, the situation is completely reversed as in the case of the studies by Zollini et al. [16] in which they also proposed a semi-automatic methodology to extract coastlines from the Sentinel-1 SAR image. This experimental algorithm, called J-Net Dynamic, was tested at two pilot sites. The statistical parameters are obtained from the distances between the Sentinel-1 coasts and the GNSS reference points, and the accuracy achieved is approximately 30 m for all images, with a minimum of 29.9 m and a maximum value of 35.9 m. Remaining in the sector of the Earth observation from space, Tuan et al. in 2018 [17] analyzed the accuracy of coastlines extracted from optical satellite images using as its reference a practical shoreline

obtained with an in situ survey. They applied three water indices to Landsat 8 OLI images, specifically, Normalized Difference Water Index (NDWI), Modified Normalized Difference Water Index (MNDWI), and Automated Water Extraction Index (AWEI). The experiments revealed that the best performing approach (AWEI) achieves an *RMSE* of 12.4 m. Finally, with the use of much more expensive remote sensing technology such as LiDAR, the results become better again; an example is the study by Yousef and Iftekharuddin [18] in which a new algorithm is proposed to extract coastlines from digital elevation models of LiDAR (DEM) fused with aerial imagery. LiDAR data and aerial imagery are fused together to maximize the information in use. The algorithm used for information extraction is the Support Vector Machine (SVM) classifier. The SVM-based approach has an average coastline position error of 2.37 m. The studies mentioned above highlight the multiplicity of techniques available for the acquisition of the coastline and the variability of the accuracies that can be obtained. In addition, the choice of the dataset is of fundamental importance and depends on the type of use made of it. Nowadays, the presence of many different data with the further possibility of acquiring others requires an in-depth analysis of the limitations or advantages that this entails. Specifically, in the case of optical remote sensing, these datasets, despite referring to the same scene, appear to be very different from each other not only due to the acquisition method but also the geometric resolution and the multispectral bands available. Hence, the aim of this work is to evaluate the accuracy in coastline extraction through the use of different datasets involving UAV/photogrammetric and satellite ones.

The experiments are carried out using RGB images of a UAV drone and on Landsat-9 and Sentinel-2 satellite images. The study area considered is the public beach of Gdynia (Poland) located on the Gulf of Gdansk. For each dataset, the supervised classification method maximum likelihood classification and subsequent automatic vectorization are applied. Furthermore, the coastlines are also extracted by manual vectorization through photointerpretation on the RGB color composition.

In order to have a very precise comparison for the evaluation of the position of each extracted line, the dataset of points obtained by surveying with a GNSS device in the RTK mode is used. Finally, two evaluation methods are applied, one involving the distance between the extracted line and a reference coastline and one of thematic accuracy. All operations are performed using Quantum GIS (QGIS) version 3.28 and ArcGIS software version 10.8.

This paper is organized as follows. Section 2 describes the study area analyzed, the datasets used, and the methodology applied for coastline extraction. Section 3 presents the results achieved by commenting and comparing with other results present in the literature. Section 4 completes the paper, summarizing its main conclusions.

2. Materials and Methods

2.1. Study Area

The study area is Downtown beach (Śródmieście) located in the city of Gdynia, which is on the northern coast of Poland, on the Baltic Sea (Figure 1). The beach is near the tourist port of Mariusz Zaruski. This waterbody has a typically sandy coastline and is approximately 400 m long. This stretch of coast is subject to recession, and in the past, in the second half of the 19th century, it was estimated that it was 2 m, while currently, it is around 1 m per year [19]. Throughout history, the coasts of Gdynia and many other coastal areas of the Baltic Sea have suffered events such as floods, storms, and erosion. These phenomena are common in these regions and may be accentuated by climate change. In particular, the Baltic Sea is known for its seasonal variations and winter storms can cause coastal erosion and flooding. Instead, the depths starting from the dry bath increase linearly with the presence of shallows and depressions that appear from the 1 m isobath. Furthermore, it should be noted that this body of water is subject to nourishment by local authorities, with a continuous consequence of changes in the seabed and the coastal environment in general.

Finally, the transparency of the water is approximately 2 m depending on the degree of visibility of the Secchi disk [20].

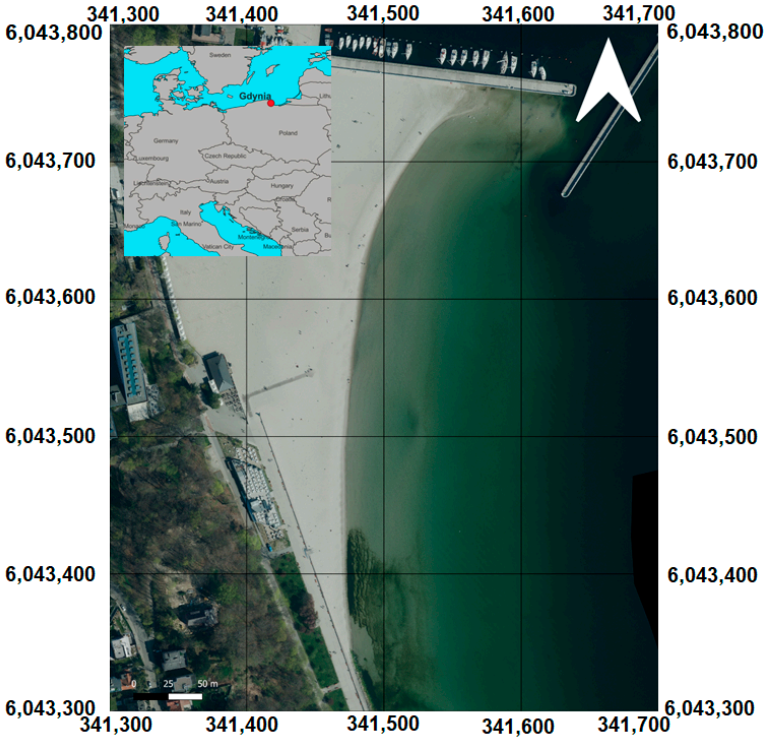

Figure 1. The location of the study area: the RGB true color composition of the orthophoto in UTM/WGS 84 zone 34N (EPSG: 32,634) coordinates expressed in meters.

Long-term measurement research was conducted at 35 stations in the Baltic Sea [21] in which it was highlighted that this sea is not subject to tides as the differences in the water level due to the impact of the tides are negligible. In particular, the minimum tide recorded in the eastern part of the Bay of Gdansk (Baltiysk, Russia) was 3.5 cm, while the maximum was in the Gulf of Finland (Gorniy Institute, Kronstadt, Russia) and was approximately 18 cm. Furthermore, the differences in water levels were found to be very few centimeters (if not almost zero) for the Baltic Sea between consecutive measurements at the same stations. Therefore, the influence of tides on water level fluctuations in Gdynia can be considered insignificant [2].

2.2. Measurement Equipment and Dataset

2.2.1. GNSS RTK Measurements

Coastline measurements using the Global Navigation Satellite System (GNSS) Real Time Kinematic (RTK) [22] method were carried out on 5 September 2023 on the waterbody at the public beach in Gdynia. Hydrometeorological conditions are an important factor influencing the obtained results, hence the shoreline surveys were conducted in windless weather and at the water level of 0 on the Douglas scale (no currents or waves). The research used the GNSS RTK Trimble R10 receiver, which is designed to collect high-precision geodetic and topographic data. This receiver allows us to receive satellite signals from all possible GNSS systems: BeiDou Navigation Satellite System (BDS), Galileo, GLObal NAvigation Satellite System (GLONASS), and Global Positioning System (GPS). Thanks to the RTK module built into the GNSS receiver, it enables measurements to be carried out with accuracies of 8 mm + 1 ppm Root Mean Square (RMS) in the horizontal plane and 15 mm + 1 ppm RMS vertical plane in real-time. For the purposes of coastline surveys, the GNSS RTK Trimble R10 receiver was mounted on a 2 m survey pole. Additionally, this pole was fitted with a special ferrule that allows it to be positioned on the bottom without

penetrating it with the sharp tip. During the research, 63 shoreline points were determined, spaced every few meters from each other (Figure 2). The geographic coordinate system of acquisition was WGS84, transformed into metric coordinates in PL-Universal Transverse Mercator (UTM) (34N zones). The choice to use this coordinate system is dictated by the easy and direct comparison with the satellite images that are already provided in WGS84/UTM zone 34. Furthermore, the geoid model used to determine the elevations is PL-EVRF2007-NH [23]. The acquired points were located at the boundary between land and sea during the measurements. The coastline course was determined with an average 2D position error of 6.4 cm and a mean height error of 5 cm. The shoreline marked out using the GNSS RTK method served as a reference line against which the errors in determining its course were determined with the use of Unmanned Aerial Vehicle (UAV) and satellite methods.

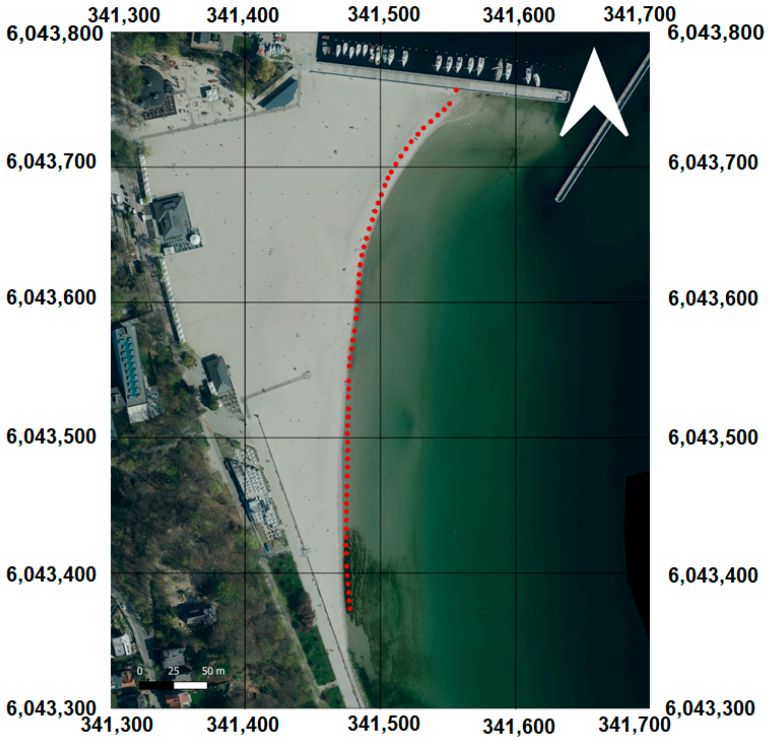

Figure 2. Shoreline points determined using the GNSS RTK method in UTM/WGS 84 zone 34N (EPSG: 32,634); coordinates expressed in meters.

2.2.2. Photogrammetric Surveys Using a UAV

In parallel with the coastline measurements using the GNSS RTK method, photogrammetric surveys with the use of a UAV were conducted on the waterbody at the public beach in Gdynia. Their effect was to determine the shoreline based on an orthophotomap generated on the basis of images taken by a photogrammetric camera mounted on a drone [24]. Firstly, it was assessed whether the meteorological conditions prevailing in the studied waterbody were suitable for carrying out photogrammetric surveys using a UAV [25]. On 5 September 2023, there were appropriate meteorological conditions, i.e., no precipitation, windless weather (wind speed not exceeding 6–7 m/s), and sunny day. Such conditions allowed clear, evenly lit photos to be taken [26]. Before starting the research, a photogrammetric control network was designed in order to georeference images taken by a drone. It consisted of 8 GCP that were evenly distributed over the studied waterbody. Following the deployment of georeference points, their geometric centers were determined using a GNSS RTK receiver. After completing the above activities, it was possible to start carrying out photogrammetric surveys using the Aurelia X8 Standard LE octocopter, on which a camera (Sony A6500 + Sony E 35 mm f/1.8 OSS) with a gimbal (Gremsy T3V3) was mounted. The measurements were conducted at a speed of approx. 25 km/h at a height of 70 m

along 10 flight profiles parallel to the coastline and spaced 10 m apart. This allowed us to obtain almost 100% longitudinal and transverse coverage of the photos [27]. As a result of photogrammetric surveys, 130 UAV images were taken with a Ground Sample Distance (GSD) not exceeding 1 cm. After completing the measurements, the recorded data were processed using the Pix4Dmapper software (version 4.8.0). Based on the Exchangeable Image File Format (EXIF) data contained in the photos, the program selected the coordinate system in which the images were originally recorded. The photos were recorded in the World Geodetic System 84 (WGS-84). Therefore, it was possible to read the approximate location of the images. The next stage of work consisted of georeferencing photos based on 8 GCPs determined with a GNSS RTK receiver [28]. It should be stated that the images taken by the drone have a high degree of accuracy. The Root Mean Square (RMS) of the differences between the coordinates of georeference points indicated on the photos and the coordinates of GCPs determined by a GNSS RTK receiver were several centimeters for the easting, northing, and normal height. After georeferencing the images, an accurate and high-resolution orthophotomap was generated for the coastal zone of the waterbody at the public beach in Gdynia (Figure 3).

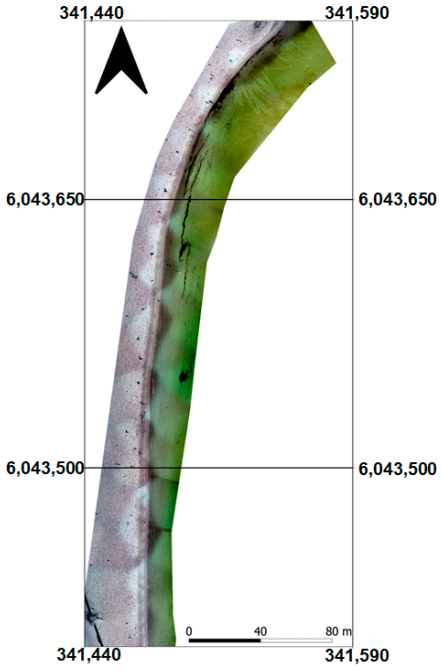

Figure 3. UAV image: the RGB true color composition in UTM/WGS 84 zone 34N (EPSG: 32,634); coordinates expressed in meters.

2.2.3. Landsat 9 OLI

The Landsat 9 Operational Land Imager (OLI) is the ninth member of the satellite series that is part of the Landsat program. It is the product of a collaboration between NASA and the U.S. Geological Survey. This satellite was successfully launched in late September 2021. Landsat satellites are known for their importance in collecting data such as Earth mapping, natural resource management, environmental monitoring, and science. Landsat-9 is in a sun-synchronous orbit near the pole at an altitude of 705 km, with an inclination of 98.2°. It completes one revolution around the Earth every 99 min, resulting in a revisit time of 16 days [29]. However, because Landsat-9 operates together with Landsat-8 at 180°, the revisit time is reduced to 8 days [30].

The two instruments supplied to Landsat 9, namely the Operational Land Imager-2 (OLI-2) and the Thermal Infrared Sensor-2 (TIRS-2), are very similar to those mounted on the previous Landsat-8 satellite, which ensures data continuity. Finally, the substantial difference is given by the radiometric resolution which goes from 12 bits (Landsat-8) to 14 bits. We also find the similarity in the spectral resolution and geometric resolution of the

bands. In fact, the OLI-2 is composed of 9 bands with a resolution of 30 m except for the panchromatic which is 15 m, and finally, the TIR-2 has two thermal bands with a resolution of 100 m [31].

Three types of data collection are available from Landsat-9 mission: real time, level 1, and level 2. The first is the raw data just acquired, and level 1 is radiometrically calibrated and orthorectified using ground GCPs and DEM data to correct for relief displacement; thanks to the high quality of this level, it allows the analysis of time series at the pixel level. Finally, level 2, derived from level 1, provides surface reflectance and surface temperature scene-based products. These last two levels have a required geometric accuracy of 12 m [32].

For this study, we use images (level 2) acquired on 2 September 2023, from a clip of the original dataset, which covers the entire affected area, as shown in Figure 4.

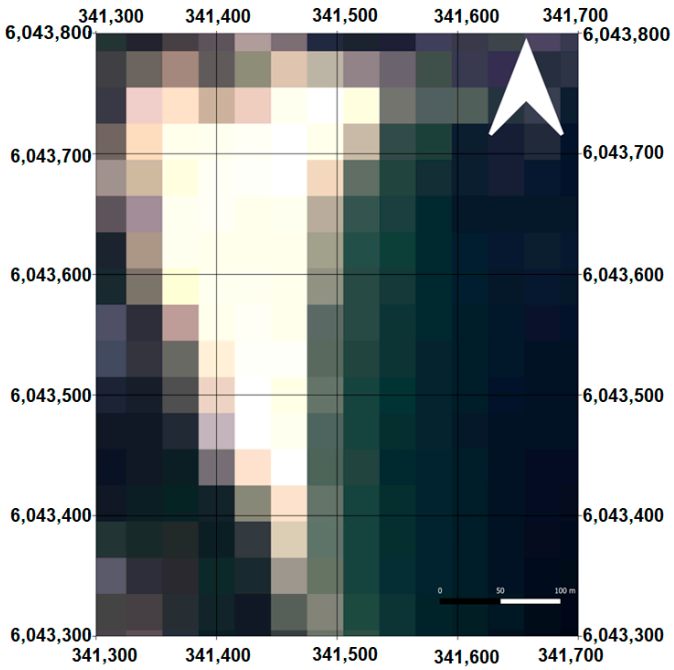

Figure 4. Landsat-9: the RGB true color composition of the satellite image in UTM/WGS 84 zone 34N (EPSG: 32,634); coordinates expressed in meters.

2.2.4. Sentinel-2

Sentinel-2 is a series of Earth observation satellites operated by the Copernicus program, starting from an initiative of the European Union in collaboration with the European Space Agency (ESA) [33]. The Copernicus Sentinel-2 mission is designed to collect high spatial and spectral resolution data for diverse purposes such as environmental surveillance, Earth resource monitoring, and other scientific and operational objectives.

It is composed of a constellation of two identical satellites, called Sentinel-2A (S2A) and Sentinel-2B (S2B), 180° out of phase, launched, respectively, on 23 June 2015 and 7 March 2017. They are designed to acquire 13 multispectral bands, whose geometric resolution is variable and goes from 10 m to 60 m. In summary, at 10 m, there are the visible bands (they are also resampled at 20 m) and the near infrared (NIR) band [34]. The short-wave infrared (SWIR) bands are at 20 m (from band 5 to 8A), and finally, the thermal bands are at 60 m.

Also, for Sentinel-2 mission, different types of data collection are available; the highest level is called level-2 and includes an atmospheric correction, Top-Of-Atmosphere (TOA), applied to Level 1C orthoimage products. Level-2 is a surface reflectance product with atmospheric correction of the orthoimage. The absolute geolocation estimates for the Sentinel-2 products, as reported in the "Data Quality Report" [35] given by the same manufacturer, show an absolute geolocation error of 7.1 m for S2A and 5.6 m for S2B.

For this study, only bands (level-2, S2B) with a geometric resolution of 10 m are used, acquired on 7 September 2023. Lastly, a clip of the study area is taken, as shown in Figure 5.

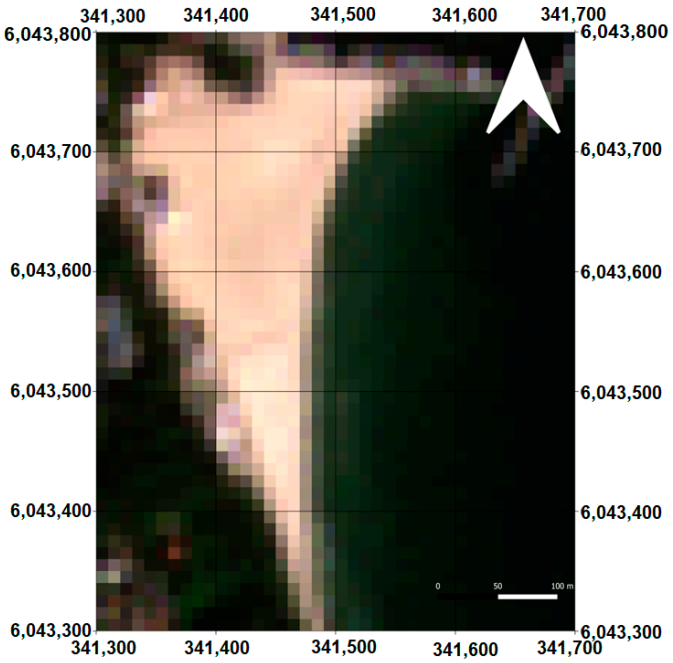

Figure 5. Sentinel-2: the RGB true color composition of the satellite image in UTM/WGS 84 zone 34N (EPSG: 32,634); coordinates expressed in meters.

2.3. Methods for Coastline Extraction

The workflow followed to extract the coastline from satellite images is shown in Figure 6.

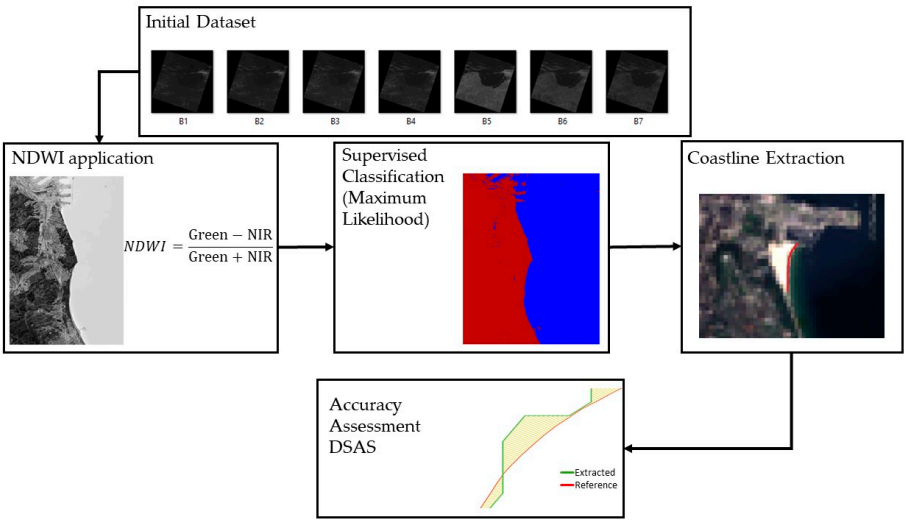

Figure 6. Workflow of the methodology used in this work for satellite dataset.

Once the image has been downloaded from the dedicated portal, we proceed with the clip of the interested area. As reported in the literature, the best way to separate waterbodies from the rest of the scene is through the use of indices. In this work, an index named Normalized Difference Water Index (NDWI) is chosen. Subsequently, the supervised classification called maximum likelihood is used to determine whether a pixel belongs to a certain class (in this case, two classes are used, water and no water).

Once the thematic map is obtained, we proceed with the automatic vectorization and subsequent extraction of the separation line between these two features. Finally, to

determine the accuracy of the results, we use an ArcGIS plugin, called Digital Shoreline Analysis System (DSAS), which allows us to obtain the mean deviations between the extracted coastline and the reference one. Furthermore, the thematic accuracy was also assessed through the use of the confusion matrix.

In the case of the UAV image, since it only provides the visible bands, the workflow is similar except in the phase of using the water index, we directly use the three available bands (RGB) to classify, as illustrated in Figure 7.

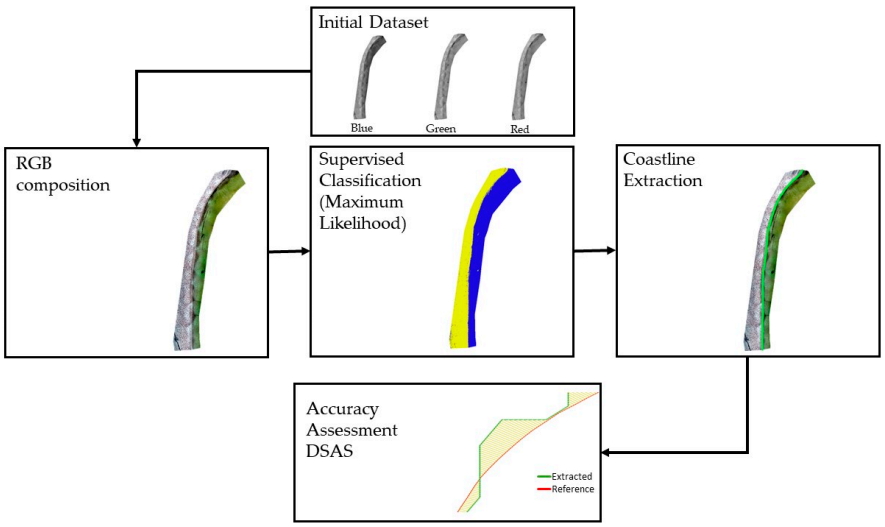

Figure 7. Workflow of the methodology used in this work for UAV dataset.

2.3.1. Normalize Difference Water Index

To support classification methods, the use of indices is often required, the best known in coastline extraction is the Normalized Water Difference Index (NDWI). The NDWI is used to highlight the water feature in a satellite image, allowing a body of water to "stand out" from other features [36].

NDWI is calculated using the combination of visible green and near infrared, as shown in the following formula:

$$\text{NDWI} = \frac{\text{Green} - \text{NIR}}{\text{Green} + \text{NIR}} \quad (1)$$

The NDWI index was proposed by McFeeters in 1996 [37]. Its main use is to detect and monitor waterbodies, such as rivers, lakes, and oceans.

Waterbodies have values greater than 0.5; in vegetation, however, they are much smaller, which allows these two classes to be distinguished more easily. This is because using the infrared band, the water reflects almost no light, while for the vegetation, we have the reflectance peak compared to the other bands.

In general, the NDWI values correspond to the following:

- Values from 0.2 to 1 are water surface;
- Values from 0.0 to 0.2 are flooding, humidity;
- Values from –0.3 to 0.0 are moderate drought, non-aqueous surfaces;
- Values from –1 to –0.3 are drought, non-aqueous surfaces [38].

Whenever it is necessary to detect a waterbody, outline its contours on the map, and monitor changes in its clarity, the NDWI index is applied.

The water index considered is applied to the Landsat-9 and Sentinel-2 datasets, producing two NDWI maps. Since the NIR band is not present in the UAV image dataset, it is not possible to apply this water index.

2.3.2. Maximum Likelihood Classification

Pixel-based classification methods allow pixels to be grouped into distinct classes based solely on spectral information. They are widely used in many fields, such as burned area detection, road extraction, coastline extraction, and other feature extraction. To obtain classes, statistical information from selected samples, called Training Sites (TS), are necessary. The coastline can be extracted based on the water and land classification using the maximum likelihood classifier which is one of the best performing methods.

The maximum likelihood classification, based on Bayesian theory, calculates for each class the probability that the pixel belongs to it given the attribute values [39]. This approach uses statistical values to assign classes to pixels in a remotely sensed image; it is necessary to initially have a series of information, such as sample pixels that are known to belong to a class, i.e., the TS. The maximum likelihood classification algorithm is trained using TS with spectral information. The algorithm learns to recognize patterns that connect image features to the subject classes. Once trained, for each pixel in the image, the classifier calculates the probability that it belongs to a certain class.

Therefore, maximum likelihood classification is based on the a posteriori probability for a pixel with a BV value to belong to class i, as shown by the following formula:

$$P(i|BV) = \frac{P(BV|i)P(i)}{P(BV)} \tag{2}$$

where *P(i)* is the prior probability of a class occurring in the study area, and *P(BV | i)* is the likelihood function. Finally, *P(BV)* is the total probability given by

$$P(BV) = \sum_{i=1}^{n} P(BV|i) \cdot P(i) \tag{3}$$

where n is the number of classes. The class with the highest a posteriori probability is assigned to that pixel [40].

Maximum likelihood classification is applied to the three types of datasets. The thematic maps produced by applying this classifier are submitted to automatic vectorization, producing three different coastlines.

2.3.3. Accuracy Assessment

The accuracy evaluation is performed for each extracted coastline. To verify the positional accuracy of each line, it is necessary to compare it with a reference one. In this study, we compared each selected coastline with that obtained in a field survey with the GNSS device.

In particular, a plugin present in ArcGIS called Digital Shoreline Analysis System (DSAS) is used. It is considered one of the most efficient, as it is able to estimate the deviation statistics between multiple lines [41]. Starting from a reference line, also called baseline, DSAS generates orthogonal transects [42] that intersect the line under examination, in this case the extracted coastlines. The distance measurements between the intersections of the transect/extracted coastline and baseline are then used to calculate the statistical values. In our study, six coastlines are extracted, of which three are through the application of maximum likelihood classification and automatic vectorization and three with direct manual vectorization on the RGB composition. The plugin allows you to choose the distance between the transects, which in this case is set at 1 m, obtaining approximately 400 transects for each coastline examined. In this way, the minimum, maximum, mean, standard deviation (σ), and Root Mean Square Error (*RMSE*) values are obtained.

The following formulas were used to calculate σ and *RMSE*:

$$\sigma = \sqrt{\frac{\sum_{i=1}^{N}(x_i - \mu)^2}{N}} \tag{4}$$

$$RMSE = \sqrt{\frac{1}{N}\sum_{i=1}^{N} {x_i}^2} \quad (5)$$

where x_i is each value obtained, i.e., the distance between the baseline and the extracted line obtained from the transects, μ is the mean, and N is the number of observations in the sample.

In order to evaluate whether the coastline extraction method meets the requirements dictated by the International Hydrographic Organization (IHO) [43], the confidence level is taken into consideration. In the context of the IHO standard, this value does not take on strictly statistical meaning, but is defined as the 95% confidence level for horizontal position, or 2D, ($R95(2D)$) as in the following formula:

$$R95(2D) = 2.45 \cdot \sigma \quad (6)$$

Furthermore, Total Horizontal Uncertainty (THU) is defined, the value of which allows the radial distribution of errors with respect to the real value (or taken as a reference) to be described with a single number. By calculating the $R95(2D)$ value, it is possible to establish which order each extracted coastline belongs to. The two most severe orders are highlighted, the "Exclusive order" (THU of 5 m with a confidence level of 95%) and the "Special order" (THU of 10 m with a confidence level of 95%).

Thematic accuracy is another very useful tool for verifying the goodness of the classification and, in this case, the successful execution of the coastline extraction. Starting from the coastline obtained via the GNSS device, it divides the scene into a water area and a no-water area. Then, we proceeded to obtain a buffer around the reference coastline, in such a way as to obtain two large test sites. Through the test sites, we proceed with the construction of the Confusion Matrix (CM), which is known as a powerful tool that allows us to determine and quantify the success of the classification.

The CM is structured as a table of values, in which the columns represent the predicted values, and the rows represent the real values, while the diagonal represents the values of the correctly classified pixels. Starting from CM, it is possible to calculate three accuracy values that permit this table to be summarized, called User Accuracy (UA), Producer Accuracy (PA), and Overall Accuracy (OA) [44].

The first, UA, refers to the probability that a pixel assigned as a determined class in the map really belongs in this class. For a generic class, j is given by the following formula:

$$UA_j = \frac{NA_j}{PC_j} \quad (7)$$

where NA_j is the number of accurately classified pixels of j, and PC_j is the number of the pixels that are classified into class j.

The PA refers to the probability that a given feature of an area on the scene is classified as such. For a generic class j, it is expressed as follows:

$$PA_j = \frac{NA_i}{PB_i} \quad (8)$$

PB_j is the total pixels belonging to the class considered.

Finally, the OA denotes the total classification accuracy:

$$OA = \frac{NA_j + NA_k + \ldots + NA_l}{P} \quad (9)$$

The numerator is the sum of pixels correctly classified for each class (j,k...,l), while the denominator is the total number of pixels used.

3. Results and Discussion

3.1. NDWI Application

In this section, applications of NDWI for selected satellite images are shown. In particular, for Landsat-9, it is shown in Figure 8, together with a zoom on the interested area, and for Sentinel-2, it is displayed in Figure 9, with a zoom thereof.

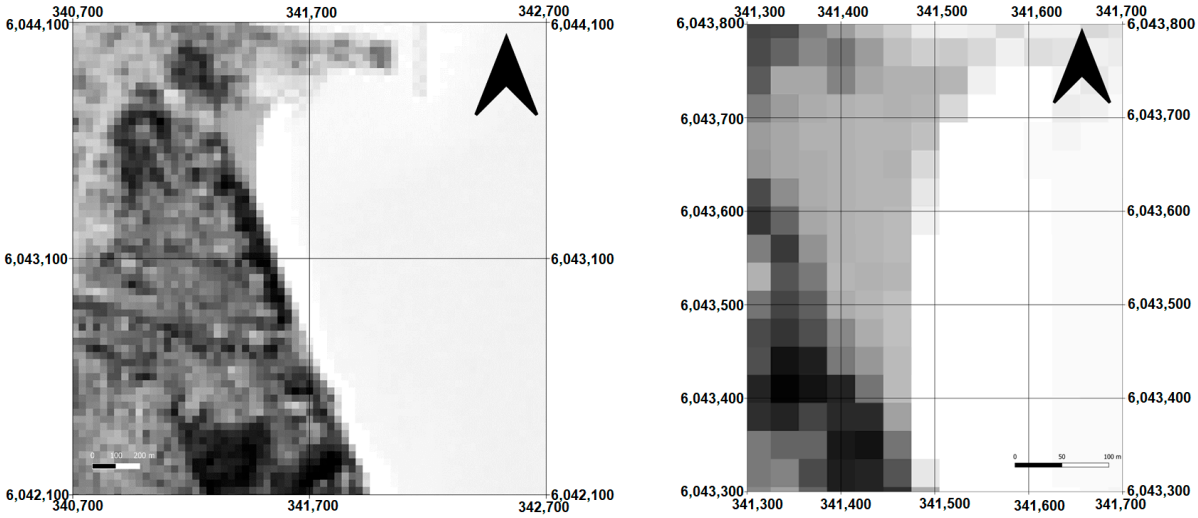

(**a**) (**b**)

Figure 8. NDWI application Landsat-9: (**a**) extended area; (**b**) zoom area.

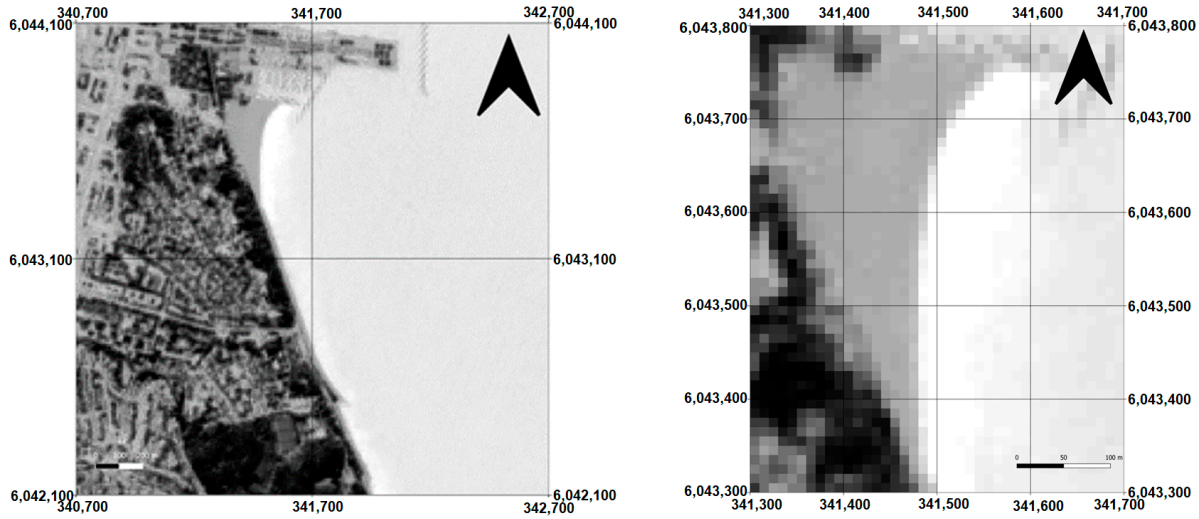

(**a**) (**b**)

Figure 9. NDWI application on Sentinel-2: (**a**) extended area; (**b**) zoom area.

3.2. Supervised Classification Application and Coastline Extraction

Following the application of supervised classification and automatically coastline vectorization, this section shows the three thematic maps (the water in blue and the not water in yellow) and the respective coastlines obtained. In particular, Figure 10 shows the classification on the UAV survey, with the corresponding extracted line, Figure 11 displays the classification on the NDWI map obtained for the Landsat-9 images and the related extracted coastline, and finally, Figure 12 is the result of the classification on the NDWI with the Sentinel-2 dataset and the obtained coastline. We remind you that for the application

on UAV images, the classification took place directly on the RGB composition and not on the NDWI map due to the non-presence of the NIR band.

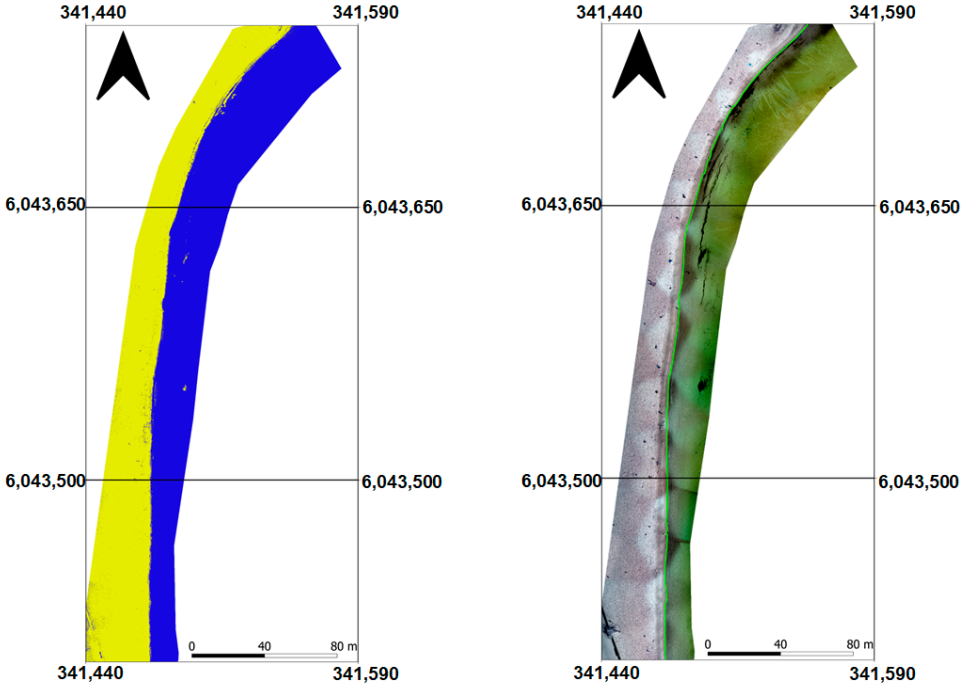

Figure 10. UAV dataset: (**a**) thematic map (water in blue, not water in yellow); (**b**) extracted coastline.

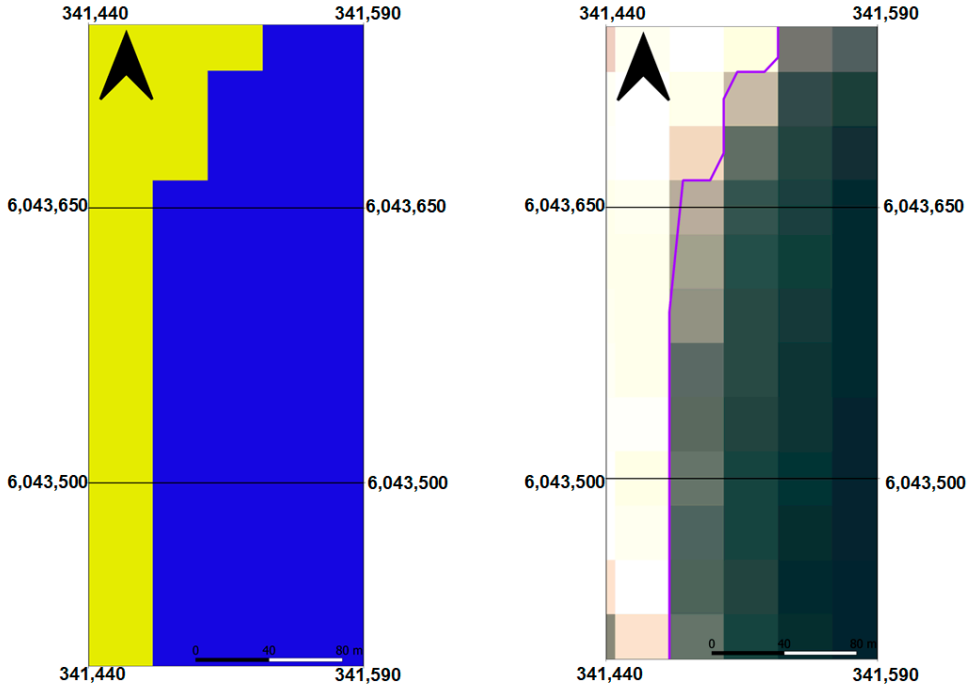

Figure 11. Landsat-9 dataset: (**a**) thematic map (water in blue, not water in yellow); (**b**) extracted coastline.

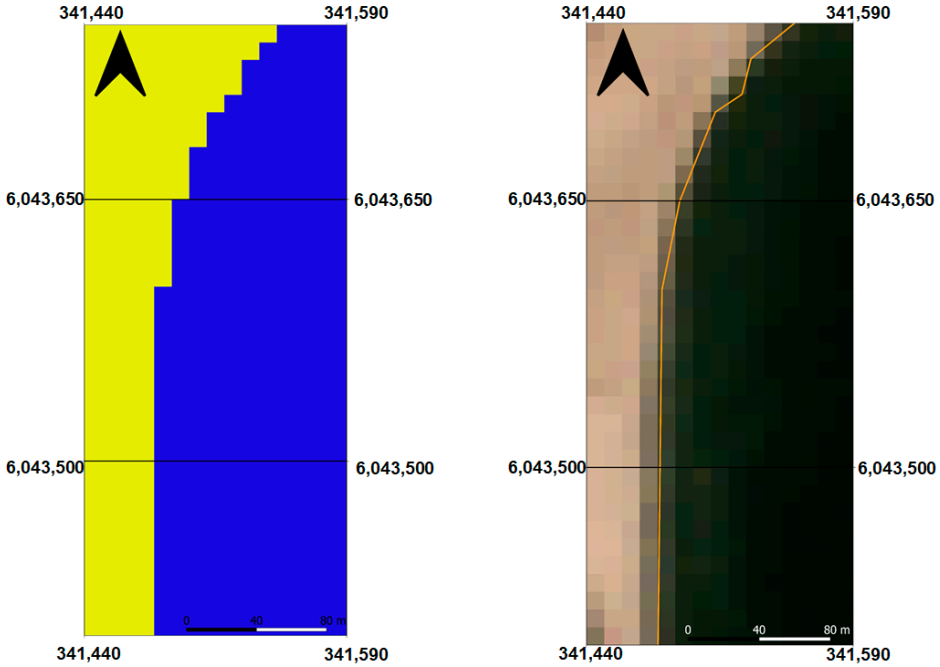

Figure 12. Sentinel-2 dataset: (**a**) thematic map (water in blue, not water in yellow); (**b**) extracted coastline.

All of the extracted coastlines have undergone a smoothing and simplification process in order to remove jaggedness given by the pixel.

3.3. Accuracy Assessment

Table 1 shows the statistical values obtained by applying the DSAS, for the three coastlines extracted using supervised classification methods. In particular, for each line examined, approximately 400 transects are generated with an equidistance of 1 m from each other.

Table 1. Statistical values of DSAS for the extracted coastlines using supervised classification approach.

Dataset	Min (m)	Max (m)	μ (m)	σ (m)	*R*95(2*D*) (m)	*RMSE* (m)
UAV	0.000	1.142	0.332	0.229	0.561	0.403
Landsat-9	0.002	18.416	3.732	3.769	9.234	5.305
Sentinel-2	0.013	8.945	3.841	1.997	4.892	4.329

In order to carry out an accuracy assessment, the geometric resolution of each dataset used is considered. It should therefore be noted that the UAV images have a pixel size of 3 cm, 30 m for Landsat-9 and finally 10 m for Sentinel-2.

As the resolution increases, the results are very different. For satellite data, the best, with an *RMSE* equal to 4.329 m, is the coastline extracted by Sentinel-2. The maximum shift with the reference line is approximately 8.9 m, below the geometric resolution of this dataset. For the Landsat-9, despite having a worse *RMSE* (5.305 m) compared to the Sentinel-2, in relation to the pixel size, they have an error of approximately one-sixth (i.e., 0.176), while for the Sentinel-2, they are more than double this value (0.432 m). In other words, in proportion to the geometric resolutions of the dataset used, Landsat-9 has a smaller error than Sentinel-2. Finally, the coastline extracted from the UAV images has an *RMSE* of 0.403 m, proving to be the best.

Figures 13–15 show the coastlines extracted from the three datasets (UAV, Landsat-9, Sentinel-2), the reference coastline (GNSS device), and the transects obtained with the DSAS plugin. Furthermore, for each dataset, a detail of the affected area is shown.

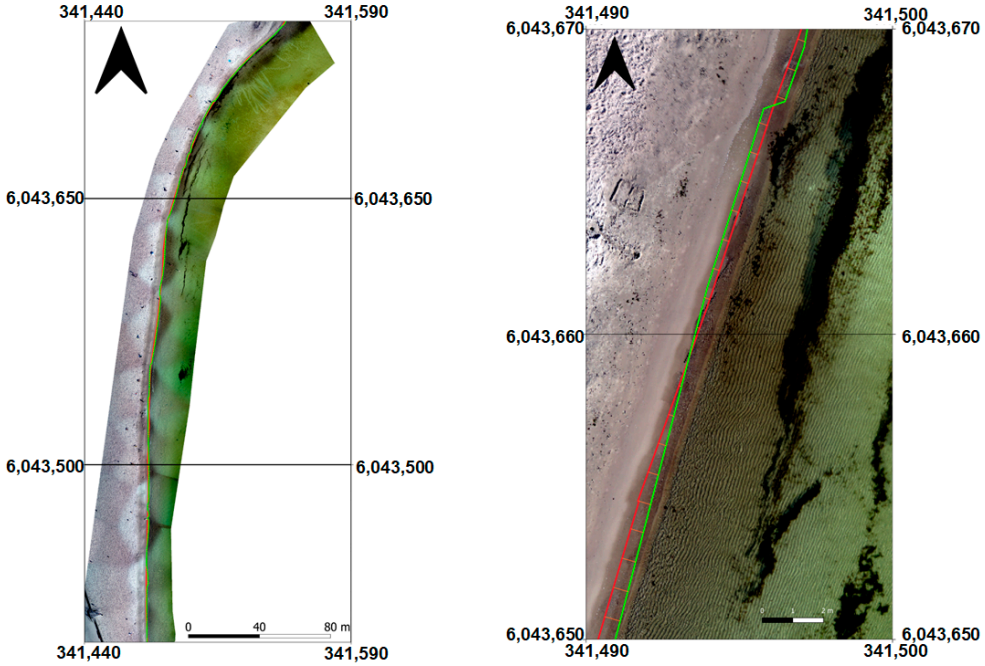

Figure 13. UAV dataset: (**a**) entire area (the extracted line in green, the reference line in red); (**b**) zoom.

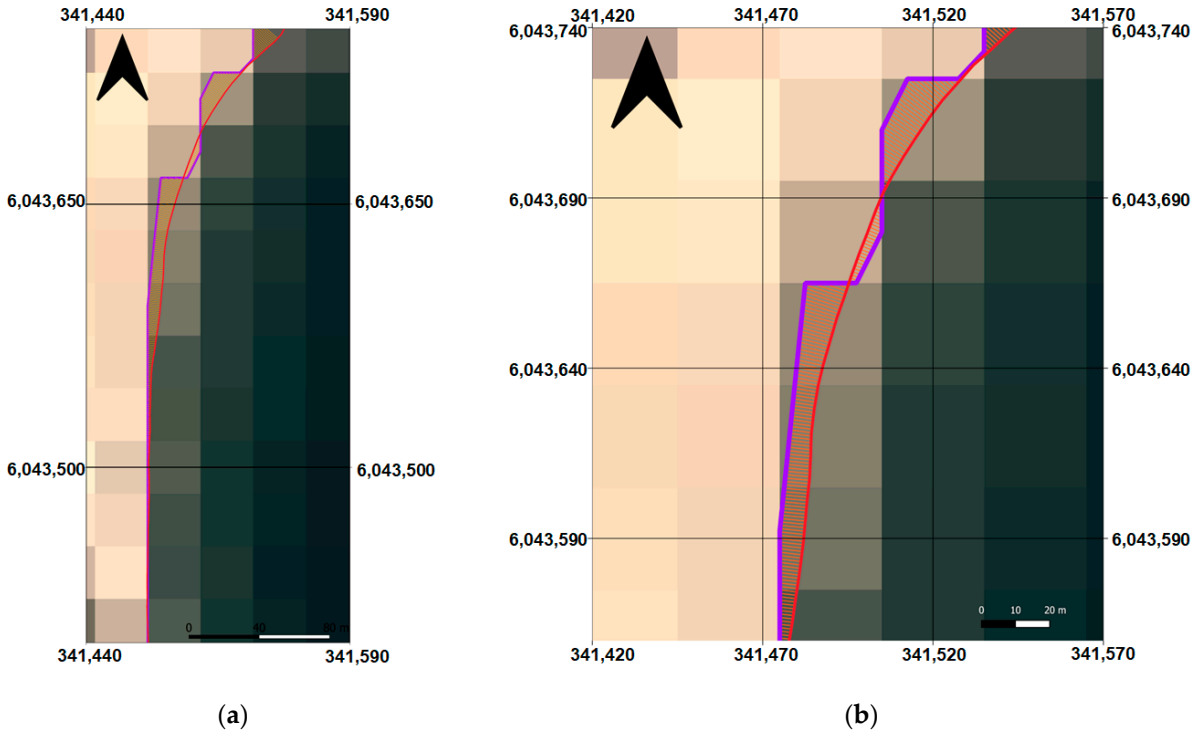

Figure 14. Landsat-9 dataset: (**a**) entire area (the extracted line in violet, the reference line in red); (**b**) zoom.

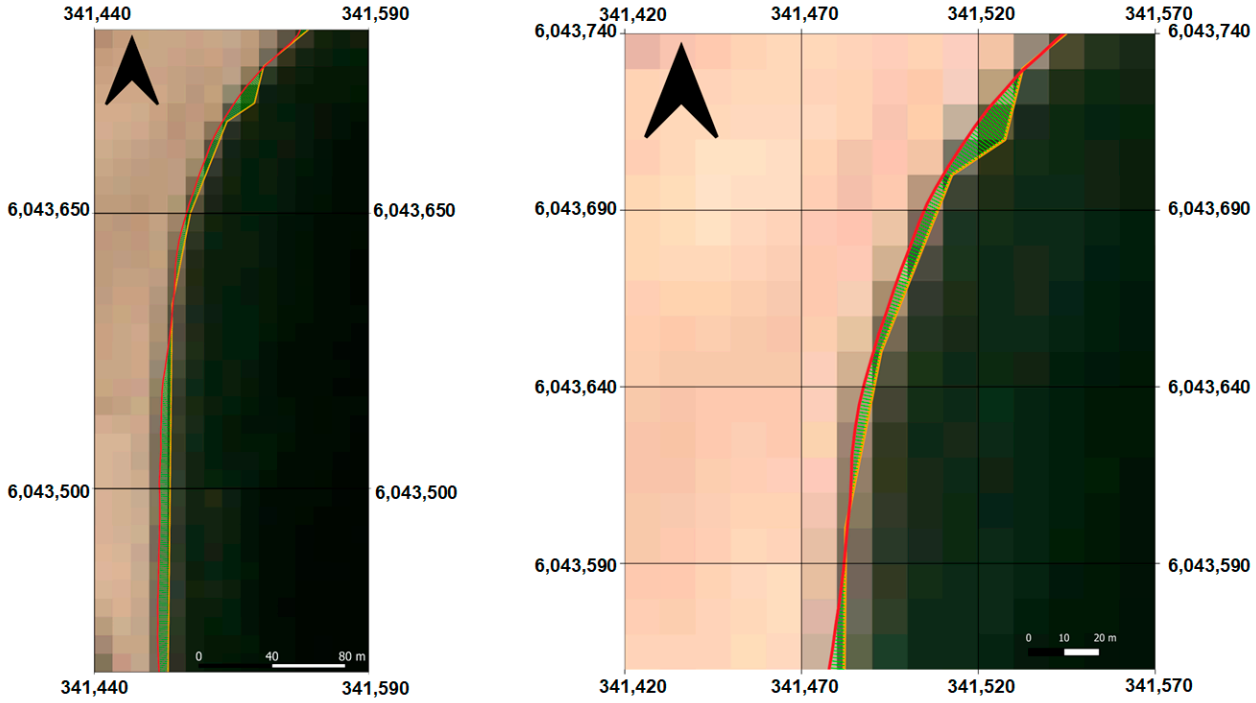

(**a**) (**b**)

Figure 15. Sentinel-2 dataset: (**a**) entire area (the extracted line in yellow, the reference line in red); (**b**) zoom.

Table 2 shows the statistical parameters, from the comparison between the reference line and the coastline extracted by manual vectorization (MV) on the RGB composition of each dataset.

Table 2. Statistical values of DSAS for the extracted coastlines using manual vectorization approach.

Dataset	Min (m)	Max (m)	μ (m)	σ (m)	*R*95(2*D*) (m)	*RMSE* (m)
UAV-MV	0.000	1.140	0.332	0.218	0.534	0.397
Landsat-9-MV	0.017	17.552	4.170	2.986	7.315	5.129
Sentinel-2-MV	0.010	6.581	3.028	1.774	4.263	3.510

The values obtained, although better, differ slightly from the previous ones, which are obtained through a classification process and consequent automatic vectorization. As you can see, the ranking from best to worst remains unchanged. The UAV dataset is still the best, the second is that of the Sentinel-2, which improves the *RMSE* by about one meter (3.510 m), and finally, the Landsat-9 dataset is the worst. However, this process is considered to be time consuming and is often subject to operator errors [45].

Table 3 shows the thematic accuracy values for the datasets used in this work and classified with the maximum likelihood classification method. The OA accuracy values close to 100% indicate correct classification.

The results actually show the quality of the coastline extraction of each dataset. In fact, in this other way of evaluating accuracy, the best result is always given in the same order previously shown by the DSAS, with the UAV first with an OA of 98.3%, followed by the Sentinel-2 dataset with 97.9%, and finally the Landsat-9 with 97%.

Table 3. Thematic accuracy values to determine the classification in two classes (water, no water).

Dataset	Accuracy	Water	Water and No Water	No Water
UAV	UA	99.029%		97.561%
	PA	98.076%		98.765%
	OA		98.378%	
Landsat-9	UA	95.000%		99.456%
	PA	99.523%		94.329%
	OA		97.029%	
Sentinel-2	UA	97.5606%		98.338%
	PA	98.3762%		97.505%
	OA		97.943%	

Finally, to confirm the validity of the results obtained, other works present in the literature are examined. In the experiment led by Su and Gibeaut [46], with the aim of determining the coastal area using UAS hyperspatial RGB imagery along the southern coast of Texas, they used the maximum likelihood classification approach achieving an OA of 92%.

In the study conducted by Esendağlı et al. [47], they used the Landsat-9 dataset to extract the shoreline, through the use of different indices including the NDWI, and they obtained a mean error of 8.8 m with standard deviation of 6.6 m, which is more than double what we obtained in our work.

In the work carried out by Şenol et al. [48], they extracted the shoreline from Hersek Lagoon using Sentinel-2 satellite images and extracting this feature using the application of a water index called Modified Normalized Difference Water Index (MNDWI) with classification based on object orientation. In their application, the maximum thematic accuracy achieved is equal to 91.5%. Also, in this case, the accuracy achieved appears to be below the method we used.

4. Conclusions

The work performed on UAV-RGB, Landsat-9, and Sentinel-2 images, in the study area concerning the Gdynia beach in Poland, analyzes the accuracy of the coastline extraction with diverse datasets.

The experiments conducted on the chosen remote sensing images highlight different results in terms of accuracy. Although the data were processed in a different way, i.e., with two different coastline extraction workflows, the results are still excellent.

To establish the positional accuracy of the extracted lines, the statistical values obtained through the DSAS were used, and furthermore, through the confusion matrix, it was also possible to establish the thematic accuracy.

The first dataset analyzed, the UAV one, turns out to be the best overall among the datasets used; in fact, in terms of *RMSE*, it reaches values in the order of a centimeter, while in thematic accuracy, it has the best value analyzed in this work. Although the data acquired by drones are limited only by the visible bands, they manage to make up for this lack thanks to the greater spatial resolution.

The coastline extracted from Sentinel-2 images has a positional accuracy of 4.329 m (*RMSE*) for extraction using supervised classification and an *RMSE* value of 3.510 m with manual vectorization approach. It also reaches an overall accuracy value of 97.943%. These values are excellent when compared to the size of the cell; in fact, Sentinell-2 ranks second among the datasets used.

Finally, the last dataset used is the one coming from the Landsat-9 satellite, where the *RMSE* values are in the order of 5 m for both coastline extraction approaches, reaching a high value of thematic accuracy. This type of dataset, despite having a lower geometric resolution when compared to the other two examined, achieves really good thematic and positional accuracy values.

Another parameter examined in this work is the one dictated according to publication S-44 which defines the standard applicable to hydrographic surveys aimed at improving navigation safety carried out by the IHO. In fact, the coastlines extracted are compliant as they respect the minimum requirement terms. In particular, the coastlines extracted from UAV-RGB and Sentinel-2 images fall within the requirements of the "Exclusive Order" (5 m THU with a 95% confidence level), while the Landsat-9 coastline falls within the requirements of the "Special order" (10 m THU with 95% confidence level).

Future developments and further studies will focus on the possibility of extending the application to other satellite images, especially those that have a higher resolution than the datasets used, as well as to UAV images with multispectral bands in addition to the visible band (RGB). Finally, we will focus on evaluating further automatic classification methods or based on machine learning approaches.

Author Contributions: Conceptualization, C.P., C.S. and A.S.; Methodology, C.P., C.S. and A.S.; Validation, F.G.F. and M.S.; Formal Analysis, F.G.F. and M.S.; Investigation, F.G.F. and M.S.; Data Curation, F.G.F. and M.S.; Writing—Original Draft Preparation, F.G.F. and M.S.; Writing—Review and Editing, C.P., C.S. and A.S.; Visualization, F.G.F. and M.S.; Supervision, C.P., C.S. and A.S. All authors have read and agreed to the published version of the manuscript.

Funding: This research was funded by the National Centre for Research and Development in Poland, grant number LIDER/10/0030/L-11/19/NCBR/2020. Moreover, this research was funded from the statutory activities of Gdynia Maritime University, grant number WN/2024/PZ/05.

Data Availability Statement: Data are contained within the article.

Conflicts of Interest: The authors declare no conflicts of interest.

References

1. Toure, S.; Diop, O.; Palma, K.; Maiga, A.S. Shoreline Detection using Optical Remote Sensing: A Review. *ISPRS Int. J. Geo-Inf.* **2019**, *8*, 75. [CrossRef]
2. Marchel, Ł.; Specht, M. Method for Determining Coastline Course Based on Low-Altitude Images Taken by a UAV. *Remote Sens.* **2023**, *15*, 4700. [CrossRef]
3. Wang, J.; Wang, L.; Feng, S.; Peng, B.; Huang, L.; Fatholahi, S.N.; Tang, L.; Li, J. An Overview of Shoreline Mapping by Using Airborne LiDAR. *Remote Sens.* **2023**, *15*, 253. [CrossRef]
4. Modava, M.; Akbarizadeh, G.; Soroosh, M. Hierarchical coastline detection in SAR images based on spectral-textural features and global–local information. *IET Radar Sonar Navig.* **2019**, *13*, 2183–2195. [CrossRef]
5. Alcaras, E.; Amoroso, P.P.; Figliomeni, F.G.; Parente, C.; Prezioso, G. Accuracy Evaluation of Coastline Extraction Methods in Remote Sensing: A Smart Procedure for Sentinel-2 Images. *Int. Arch. Photogramm. Remote Sens. Spat. Inf. Sci.* **2022**, *48*, 13–19. [CrossRef]
6. Jana, A.; Maiti, S.; Biswas, A. Analysis of short-term shoreline oscillations along Midnapur-Balasore Coast, Bay of Bengal, India: A study based on geospatial technology. *Model. Earth Syst. Environ.* **2016**, *2*, 64. [CrossRef]
7. Qiao, G.; Mi, H.; Wang, W.; Tong, X.; Li, Z.; Li, T.; Liu, S.; Hong, Y. 55-year (1960–2015) spatiotemporal shoreline change analysis using historical DISP and Landsat time series data in Shanghai. *Int. J. Appl. Earth Obs. Geoinf.* **2018**, *68*, 238–251. [CrossRef]
8. Aguilar, F.J.; Fernández, I.; Pérez, J.L.; López, A.; Aguilar, M.A.; Mozas, A.; Cardenal, J. Preliminary results on high accuracy estimation of shoreline change rate based on coastal elevation models. *Int. Arch. Photogramm. Remote Sens. Spat. Inf. Sci.* **2010**, *33*, 986–991.
9. Figliomeni, F.G.; Guastaferro, F.; Parente, C.; Vallario, A. A Proposal for Automatic Coastline Extraction from Landsat 8 OLI Images Combining Modified Optimum Index Factor (MOIF) and K-Means. *Remote Sens.* **2023**, *15*, 3181. [CrossRef]
10. Kuenzer, C.; Ottinger, M.; Liu, G.; Sun, B.; Baumhauer, R.; Dech, S. Earth Observation-Based Coastal Zone Monitoring of the Yellow River Delta: Dynamics in China's Second Largest Oil Producing Region over Four Decades. *Appl. Geogr.* **2014**, *55*, 92–107. [CrossRef]
11. Ding, Y.; Yang, X.; Jin, H.; Wang, Z.; Liu, Y.; Liu, B.; Zhang, J.; Liu, X.; Gao, K.; Meng, D. Monitoring Coastline Changes of the Malay Islands Based on Google Earth Engine and Dense Time-Series Remote Sensing Images. *Remote Sens.* **2021**, *13*, 3842. [CrossRef]
12. Zhang, Y.; Li, X.; Zhang, J.; Song, D. A study on coastline extraction and its trend based on remote sensing image data mining. *Abstr. Appl. Anal.* **2013**, *2013*, 693194. [CrossRef]
13. Dominici, D.; Zollini, S.; Alicandro, M.; Della Torre, F.; Buscema, P.; Baiocchi, V. High Resolution Satellite Images for Instantaneous Shoreline Extraction Using New Enhancement Algorithms. *Geosciences* **2019**, *9*, 123. [CrossRef]

14. Goncalves, R.M.; Awange, J.L. Three most widely used GNSS-based shoreline monitoring methods to support integrated coastal zone management policies. *J. Surv. Eng.* **2017**, *143*, 05017003. [CrossRef]
15. Zanutta, A.; Lambertini, A.; Vittuari, L. UAV Photogrammetry and Ground Surveys as a Mapping Tool for Quickly Monitoring Shoreline and Beach Changes. *J. Mar. Sci. Eng.* **2020**, *8*, 52. [CrossRef]
16. Zollini, S.; Dominici, D.; Alicandro, M.; Cuevas-González, M.; Angelats, E.; Ribas, F.; Simarro, G. New Methodology for Shoreline Extraction Using Optical and Radar (SAR) Satellite Imagery. *J. Mar. Sci. Eng.* **2023**, *11*, 627. [CrossRef]
17. Tuan, T.A.; Nguyet, N.T.A.; Hong, P.V.; Ngan, N.T.A.; Le Phuong, V. Interpretation of water indices for shoreline extraction from Landsat 8 OLI data on the southwest coast of Vietnam. *Vietnam J. Mar. Sci. Technol.* **2018**, *18*, 339–349. [CrossRef]
18. Yousef, A.; Iftekharuddin, K. Shoreline extraction from the fusion of LiDAR DEM data and aerial images using mutual information and genetic algrithms. In Proceedings of the 2014 International Joint Conference on Neural Networks (IJCNN), Beijing, China, 6–11 July 2014; pp. 1007–1014.
19. Małka, A. Landslide susceptibility mapping of Gdynia using geographic information system-based statistical models. *Nat. Hazards* **2021**, *107*, 639–674. [CrossRef]
20. Specht, M.; Specht, C.; Wąż, M.; Dąbrowski, P.; Skóra, M.; Marchel, Ł. Determining the variability of the territorial sea baseline on the example of waterbody adjacent to the municipal beach in Gdynia. *Appl. Sci.* **2019**, *9*, 3867. [CrossRef]
21. Medvedev, I.P.; Rabinovich, A.B.; Kulikov, E.A. Tidal Oscillations in the Baltic Sea. *Oceanology* **2013**, *53*, 526–538. [CrossRef]
22. Baptista, P.; Bastos, L.; Bernardes, C.; Cunha, T.; Dias, J. Monitoring Sandy Shores Morphologies by DGPS—A Practical Tool to Generate Digital Elevation Models. *J. Coast. Res.* **2008**, *24*, 1516–1528. [CrossRef]
23. Council of Ministers of the Republic of Poland. *Ordinance of the Council of Ministers of 15 October 2012 on the National Spatial Reference System*; Council of Ministers of the Republic of Poland: Warsaw, Poland, 2012. (In Polish)
24. Specht, O. Multi-sensor Integration of Hydroacoustic and Optoelectronic Data Acquired from UAV and USV Vehicles on the Inland Waterbody. *Int. J. Mar. Navig. Saf. Sea Transp.* **2023**, *17*, 791–798. [CrossRef]
25. Jiménez-Jiménez, S.I.; Ojeda-Bustamante, W.; Marcial-Pablo, M.d.J.; Enciso, J. Digital Terrain Models Generated with Lowcost UAV Photogrammetry: Methodology and Accuracy. *ISPRS Int. J. Geo. Inf.* **2021**, *10*, 285. [CrossRef]
26. Lewicka, O.; Specht, M.; Specht, C. Assessment of the Steering Precision of a UAV along the Flight Profiles Using a GNSS RTK Receiver. *Remote Sens.* **2022**, *14*, 6127. [CrossRef]
27. Seifert, E.; Seifert, S.; Vogt, H.; Drew, D.; van Aardt, J.; Kunneke, A.; Seifert, T. Influence of Drone Altitude, Image Overlap, and Optical Sensor Resolution on Multi-view Reconstruction of Forest Images. *Remote Sens.* **2019**, *11*, 1252. [CrossRef]
28. Specht, O. Land and Seabed Surface Modelling in the Coastal Zone Using UAV/USV-based Data Integration. *Sensors* **2023**, *23*, 8020. [CrossRef] [PubMed]
29. USGS, Landsat-9 Mission. Available online: https://www.usgs.gov/landsat-missions/landsat-9 (accessed on 20 November 2023).
30. Masek, J.G.; Wulder, M.A.; Markham, B.; McCorkel, J.; Crawford, C.J.; Storey, J.; Jenstrom, D.T. Landsat 9: Empowering open science and applications through continuity. *Remote Sens. Environ.* **2020**, *248*, 111968. [CrossRef]
31. Landsat-9 Overview. Available online: https://landsat.gsfc.nasa.gov/satellites/landsat-9/landsat-9-overview/ (accessed on 20 November 2023).
32. Choate, M.J.; Rengarajan, R.; Storey, J.C.; Lubke, M. Landsat 9 Geometric Commissioning Calibration Updates and System Performance Assessment. *Remote Sens.* **2023**, *15*, 3524. [CrossRef]
33. Sentinel-2 Missions. Available online: https://sentinel.esa.int/web/sentinel/missions/sentinel-2 (accessed on 20 November 2023).
34. Drusch, M.; Del Bello, U.; Carlier, S.; Colin, O.; Fernandez, V.; Gascon, F.; Hoersch, B.; Isola, C.; Laberinti, P.; Martimort, P.; et al. Sentinel-2: ESA's optical high-resolution mission for GMES operational services. *Remote Sens. Environ.* **2012**, *120*, 25–36. [CrossRef]
35. Sentinel ESA Sites. Available online: https://sentinel.esa.int/documents/247904/685211/Sentinel-2_L1C_Data_Quality_Report (accessed on 27 December 2023).
36. Figliomeni, F.G.; Parente, C. Bathymetry from satellite images: A proposal for adapting the band ratio approach to IKONOS data. *Appl. Geomat.* **2023**, *15*, 565–581. [CrossRef]
37. McFeeters, S.K. The use of the Normalized Difference Water Index (NDWI) in the delineation of open water features. *Int. J. Remote Sens.* **1996**, *17*, 1425–1432. [CrossRef]
38. Normalized Difference Water Index. Available online: https://eos.com/make-an-analysis/ndwi/#:~:text=The%20Normalized%20Difference%20Water%20Index,also%20known%20as%20NDWI%20GAO (accessed on 20 November 2023).
39. Sisodia, P.S.; Tiwari, V.; Kumar, A. Analysis of supervised maximum likelihood classification for remote sensing image. In Proceedings of the International Conference on Recent Advances and Innovations in Engineering (ICRAIE-2014), Jaipur, India, 9–11 May 2014; pp. 1–4.
40. Ok, A.O.; Akar, O.; Gungor, O. Evaluation of random forest method for agricultural crop classification. *Eur. J. Remote Sens.* **2012**, *45*, 421–432. [CrossRef]
41. Mirdan, M.M.; Tolba, E.R.; Abdellah, S.; Galal, E.M. Digital shoreline analysis system techniques for stability detection: An applied case study on Port Said, Egypt. *Egypt. J. Aquat. Res.* **2023**, *49*, 460–470. [CrossRef]
42. Baig, M.R.I.; Ahmad, I.A.; Shahfahad; Tayyab, M.; Rahman, A. Analysis of shoreline changes in Vishakhapatnam coastal tract of Andhra Pradesh, India: An application of digital shoreline analysis system (DSAS). *Ann. GIS* **2020**, *26*, 361–376. [CrossRef]

43. International Hydrographic Organization Standards for Hydrographic Surveys, S-44 Edition 6.1.0. Available online: https://iho.int/uploads/user/pubs/standards/s-44/S-44_Edition_6.1.0.pdf (accessed on 20 November 2023).
44. Alcaras, E.; Amoroso, P.P.; Parente, C.; Prezioso, G. Remotely sensed image fast classification and smart thematic map production. *Int. Arch. Photogramm. Remote Sens. Spat. Inf. Sci.* **2021**, *46*, 43–50. [CrossRef]
45. Alcaras, E.; Amoroso, P.P.; Baiocchi, V.; Falchi, U.; Parente, C. Unsupervised classification based approach for coastline extraction from Sentinel-2 imagery. In Proceedings of the 2021 International Workshop on Metrology for the Sea; Learning to Measure Sea Health Parameters (MetroSea), Reggio Calabria, Italy, 4–6 October 2021; pp. 423–427.
46. Su, L.; Gibeaut, J. Using UAS hyperspatial RGB imagery for identifying beach zones along the South Texas coast. *Remote Sens.* **2017**, *9*, 159. [CrossRef]
47. Esendağlı, Ç.; Selim, S.; Demir, N. Comparison of shoreline extraction indexes performance using Landsat 9 satellite images in the heterogeneous coastal area. *Intercont. Geoinf. Days* **2022**, *4*, 199–202.
48. Şenol, H.İ.; Kaya, Y.; Yiğit, A.Y.; Yakar, M. Extraction and geospatial analysis of the Hersek Lagoon shoreline with Sentinel-2 satellite data. *Surv. Rev.* **2023**, 1–16. [CrossRef]